Proceedings of the ASME 2010 3rd Joint US-European Fluids Engineering Summer Meeting and 8th International Conference on Nanochannels, Microchannels, and Minichannels
FEDSM-ICNMM2010
August 1-5, 2010, Montreal, Canada

FEDSM-ICNMM2010-30702

TOWARDS A MODEL OF VIBRATION FOR A CANTILEVERED MIXING ROTOR

Noel Kippers
Graduate Student
Department of Mechanical Engineering
University of New Brunswick
Fredericton, New Brunswick, E3B 5A3
Email: noel.kippers@unb.ca

Gordon Holloway
Professor
Department of Mechanical Engineering
University of New Brunswick
Fredericton, New Brunswick, E3B 5A3
Email: holloway@unb.ca

Andrew Gerber
Professor
Department of Mechanical Engineering
University of New Brunswick
Fredericton, New Brunswick, E3B 5A3
Email: agerber@unb.ca

ABSTRACT

This paper presents an analytic model for a mixing shaft with a standard 45° *pitched-blade impeller (PBI) in a baffled mixing vessel. The vibrations and orbits are influenced by a combination of structural and hydrodynamic forces which are sensitive to geometric parameters, fluid properties and rotational speed. Results are included for three water-glycerol mixtures with viscosities of* 50 *cP,* 100 *cP and* 500 *cP and rotational speeds up to 1.3 time the natural frequency of the shaft with both tensile and compressive axial thrust loads resulting from the pitched blades. Experimental results for the expected mean squared vibration response, power spectral densities (PSD) and orbit statistics are presented. A model is presented that explains a number of trends that were experimental observed including asymmetry of the shaft's vibration amplitude with rotation direction.*

NOMENCLATURE

$C, \bar{C}$ Damping matrix, $\frac{kg}{sec}$
C_T Thrust coefficient
D Impeller diameter, m
D_m Mean diameter, m
D_T Tank diameter, m
E Expected mean squared response, m^2
H Transfer function
H_f Fluid height, m
I Moment of area m^4
J Polar moment of inertia, $kg * m^2$
$K, \bar{K}$ Stiffness matrix, $\frac{N}{m}$
L Rotor blade length, m
$M, \bar{M}$ Mass, kg
M_y Moment at the shaft root, N*m
M_z Moment at the shaft root, N*m
S Power spectral density, $\frac{(\ )^2}{\frac{rad}{sec}}$
T Thrust, N
W Impeller blade width, m
W_b Tank baffle width, m
$\forall$ Impeller volume, m^3
$\forall_s$ Shaft volume, m^3
c_s Structural damping, $\frac{kg}{sec}$
c_f Viscous damping, $\frac{kg}{sec}$
d_i Shaft's inside diameter, m
d_o Shaft's outside diameter, m
$f_{y,z}$ Force in y and z, N
D Impeller diameter, m
k_a Axial stiffness, $\frac{N}{m}$
k_c Internal friction stiffness, $\frac{N}{m}$
k_r Horizontal component of axial stiffness, $\frac{N}{m}$
k_s Structural stiffness, $\frac{N}{m}$
k_β Alford's stiffness, $\frac{N}{m}$
k_τ Torquewhirl stiffness, $\frac{N}{m}$
l Shaft length, m
m_f Added fluid mass, kg

m_s Impeller mass, kg
$m_s u$ Mass eccentricity, $kg*m$
r, r_0 Radial deflection, m, geometric eccentricity, m
t Time, sec
t^* $t\omega_{nb}$
y Displacement in j-direction, m
y^* $\frac{y}{D}$
z Displacement in k-direction, m
z^* $\frac{z}{D}$
α Normalized damping factor
β Alford's force coefficient
γ_1 Skewness
γ_2 Kurtosis
$\varepsilon_{y,z}$ Strain in y and z planes at roots of cantilever
ζ_s, ζ_f Structural damping ratio, viscous damping ratio
θ Angle between shaft and x-axis
λ Eigenvalue solution
μ Fluid viscosity, $\frac{kg}{m*sec}$
τ Impeller torque, $N*m$
ψ Normalized natural frequency
Ω Rotational speed, $\frac{rad}{sec}$
Ω^* Normalized rotation speed, $\frac{\Omega}{\omega_{nb}}$
ω Frequency, $\frac{rad}{sec}$
ω^* Normalized frequency, $\frac{\omega}{\omega_{nb}}$
ω_{nb} Bending natural frequency, $\frac{rad}{sec}$

INTRODUCTION

Industrial chemical reactors often include rotating agitators with different impeller geometries and tank arrangements selected for particular applications [1]. A general layout for a standard mixer design is shown in figure 1. The tank is a vertical cylinder of diameter D_T with four evenly spaced baffles that have a width W_b within the range of $\frac{T}{12} < W_b < \frac{T}{10}$ that extend the full height of the tank. The shaft is typically a vertical cantilever with an impeller mounted at the end. The shaft is supported at the root of the shaft with a series of tapered and radial bearings and seals.

Efficient mixing requires complex, three dimensional fluid flow within the reactor [2–6]. In such cases the impeller blades experience random and periodic pressure forces that can excite bending and torsional shaft vibrations. The life of shaft seals and bearings depends on the amplitude and frequency of these vibrations and therefore a practical predictive tool is required for design and maintenance planning. This paper evaluates a rotor dynamic model for the vibration of a cantilevered rotating mixing impeller based on the extension of previous studies in the literature. Model predictions will be compared to experimental data. Gyroscopic effects are neglected in the present case because of the rotor's relatively small mass polar moment of inertia.

The simplest model of rotor vibration is a linear one where the motion of the impeller mass center is confined to a horizontal plane. The differential equations describing the displacement along perpendicular axes in the plane are coupled leading to a 4th order system [7, 8]. A model of this type can be used to determine the limits of stability, natural frequency and magnitude of the vibration when subjected to periodic or random excitation forces. The assumption of linearity restricts the amplitudes of vibration that may be considered but it has been observed by Diken [9] in his study of Jeffcott rotors that a linear model can adequately predict some important vibration characteristics even in the presence of non-linearities.

Often the objective in rotor studies is to identify stability limits for shaft whirl. Cohen and Porat [10] examined the stability of a cantilever rotor driven by a flexible shaft. Khader [11] studied cantilevered shaft stability for different load conditions. Lee and Yun [12] studied the stability and natural frequency of cantilevered rotors under non-conservative torques and axial loads. The most often identified source of whirl instability is cross coupling stiffness [8] that effectively acts as a damping force that is tangent to the whirl orbit. This stiffness can originate from such sources as "torque whirl", internal damping of the shaft, or fluid forces such as Alford's force.

There has been considerable work done on modeling Alford's force acting on turbo-machinery impellers which has some relevance to the present problem. The most significant differences between the mixer and turbomachinery being the large clearances around the impeller and baffles of the mixing equipment. Storace et al. [13] experimentally investigated the Alford's force on an axial-flow compressor impeller when the axis of rotation is displaced from the static centerline of the engine structure. The resulting non-uniform clearance created a force tangential to the impeller that results from an imbalance of pressure loading on the blades. Storace et al. [13] cite it as a cause of backward whirling over a large range of operating conditions and synchronous/forward whirling near the design conditions of their compressor. Alford's force is also described by Vance [7] who reports on experiments for an axial flow impeller.

There has been very few studies done on the fluid forces acting on a mixing impeller undergoing vibrations. Exceptions are the study of Berger [14] and Mohammed et al. [15] who used finite element methods to simulate fully coupled fluid structure interaction. This type of approach is computationally very demanding and currently does not make for a practical tool of rotordynamic analysis for routine design and trouble shooting. Nevertheless, CFD can provide estimates of the fluid forces acting on the rotating impeller that can be used to formulate a practical rotordynamic tool; this approach will be explored in the present paper.

Model development requires experimental data for validation but there has been very little research done to explore the relationship between the operating conditions and the shaft vibration of pitched-blade mixing impellers. An exception is the previous study by the authors [16] which considered the effects of geometry, fluid viscosity and operating speed on shaft vibration amplitude. It was reported that the impeller orbits are random and the deflections are normally distributed. Furthermore they found that the mean square vibration amplitude increases beyond the critical speed of the rotor and that the direction of the shaft rotation affects the results. Data from this study will be presented to allow evaluation of the model formulation.

EXPERIMENTAL MIXING MODEL

Apparatus

A schematic of the model mixing tank is shown in figure 1 with dimensions given in table 1. The tank model is a standard design with a flat bottom and evenly spaced removable baffles of standard size that run the vertical length of the tank. The fluid was constrained by a lid at a height $H_L = D_T$ for all experimental trials. The impeller shaft was constructed out of a hollow cast acrylic section and was mounted in the tank in an overhung configuration and supported with two bearings at the upper end. The shaft was partially filled with tungsten powder to increase the mass and hence lower the natural frequency of the impeller without altering the geometry. The tungsten powder was placed inside the shaft with a mass center coincident with the mass center of the impeller. The impeller was dynamically balanced to a tolerance of $7.2 * 10^{-6}$ $kg * m$. The average geometric eccentricity of the shaft was 0.53 mm with a standard deviation of 0.19 mm.

A standard pitched blade impeller with four blades and the dimensions listed in table 2 was used. A schematic of the impeller is shown in figure 2.

The test fluids used were mixtures of glycerol and water which provided a range of density between 1214 $\frac{kg}{m^3}$ - 1222 $\frac{kg}{m^3}$ and a dynamic viscosity ranging from $\mu = 42$ cP - 552 cP.

Instrumentation

The cantilever shaft was fitted with three full bridge strain gages at the root to measure the bending strain in the planes normal to the axial direction of the shaft and the torsional strain about the shaft axis. The strain gages were mounted inside the rotating shaft to protect them from the test fluid. The strain gage measurements were used to infer bending and torsional deflection as well as the mean torque on the shaft. The shaft orbit was directly observed using a high-speed camera (Dantec Nano Sense MKIII) and a high intensity LED mounted at the end of the shaft. The camera and strain gage measurements were both initially triggered by the zero position of a rotary encoder. The encoder was also used to measure the shaft's rotational speed.

Data from the three strain gage channels were transmitted from the rotating shaft to the data acquisition system using an

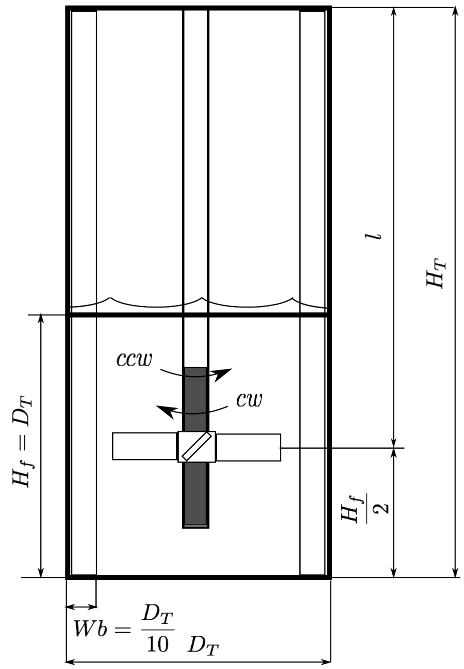

Figure 1. CROSS SECTION OF THE MIXING VESSEL WITH STANDARD NOMENCLATURE

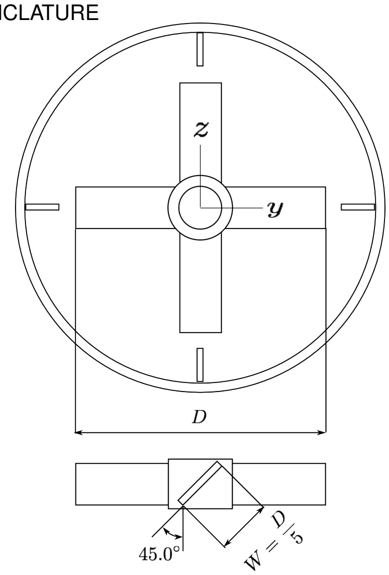

Figure 2. FOUR BLADE PITCHED-BLADE IMPELLER.

Accumetrics™ $AT-7000$ telemetry system as a 12-bit digital signal with minimal noise. Prior to transmission the signal is filtered using a 250 Hz, 8-pole elliptical filter and amplified. The strain gage signals were sampled at 500 Hz for a total of 135 revolutions. Images were recorded every 60° of rotation; at the highest rotational speed (410 rpm) images were recorded at a frame rate of 41 Hz. At this frame rate Nyquist criteria is satisfied

Table 1. MODEL PARAMETERS

Symbol	Parameter	Unit	Model
D_T	Tank Diameter	m	0.356
W_b	Baffle Width	m	0.035
H_T	Tank Height	m	0.774
H_f	Fluid Height	m	0.31
l	Length to Impeller	m	0.616
d_o	Outside Shaft Diameter	m	0.038
d_i	Inside Shaft Diameter	m	0.0318
E	Modulus of Elasticity	$\frac{N}{m^2}$	$2.38*10^9$
I	Moment of Inertia	m^4	$5.36*10^{-8}$
m_s	Shaft Mass	kg/m	0.516
k_s	Shaft Stiffness	N/m	1637
$\omega_{nb}\dagger$	Natural Frequency	$\frac{rad}{sec}$	30.1805
$\zeta_s^\dagger$	Shaft Damping Ratio		0.045
$\zeta_f^\ddagger$	Fluid Damping Ratio		0.061

† Note: Measured in air.

‡ Note: Measured in 50 and 500 *cP* test fluid.

Table 2. PROPERTIES OF THE PITCHED-BLADE IMPELLER

Symbol	Parameter	Unit	Model
#B	Blade #		4
$\frac{D}{T}$	Diameter Ratio		$\frac{5}{7}$
$\frac{c}{T}$	Clearance Ratio		0.047
D	Impeller Diameter	m	0.254
W	Blade Width	m	0.127
$m_s^\dagger$	Impeller mass	kg	1.798
J_x	Polar Moment	$kg*m^2$	$4.863*10^{-3}$
$J_y = J_z$	Polar Moment	$kg*m^2$	$3.093*10^{-3}$

†Note: Total mass of the tungsten powder and impeller

for any periodic orbit motion that has a frequency less than twice the turning rate.

The viscosity and temperature of the fluid were measured using a digital viscometer (Brookfield DV-II+) before and after each trial.

Data Processing

The bending strain measured at the root of the shaft was used to infer the impeller motion assuming a static deflection curve corresponding to a massless cantilever beam with a point load applied at the impeller's mass center. The relationship between the bending strain and deflection in the rotating frame of reference of the shaft was approximated by

$$\hat{y} = \left[\frac{\sqrt{M_y^2 + M_z^2}\,l^2}{3EI} + \frac{M_c l^2}{6EI}\right]\cos(\theta_M) \tag{1}$$

$$\hat{z} = \left[\frac{\sqrt{M_y^2 + M_z^2}\,l^2}{3EI} + \frac{M_c l^2}{6EI}\right]\sin(\theta_M) \tag{2}$$

where

$$M_y = \frac{2EI\varepsilon_y}{d_o} \quad M_z = \frac{2EI\varepsilon_z}{d_o} \tag{3}$$

while ε_y and ε_z are the measured strains, l is the shaft length, d_o is the outside diameter of the shaft, $M_c = -1.5\Omega^{*2}$ is a calibration constant used to match the strain gage and camera measurements and θ_M is the angle produced by the resultant moment vector. Deflections, $\hat{y}$ and $\hat{z}$, inferred from the strain gages were transformed to a laboratory frame of reference using the angular position, θ_E, provided by the encoder and the equations

$$y = \hat{y}\cos\theta_E - \hat{z}\sin\theta_E \tag{4}$$

$$z = \hat{y}\sin\theta_E + \hat{z}\sin\theta_E \tag{5}$$

The camera measures the position of the geometric center of the shaft, y and z in a laboratory frame of reference directly. These measurements are recorded with respect to its center of rotation. An important difference between these measurements and the values derived from the strain gages ($\hat{y}$ and $\hat{z}$) is that the camera measurements include the geometric eccentricity of the shaft while the strain gages results do not. The geometric eccentricity was determined for each trial by manually rotating the shaft while taking a slow series of images. With both the camera and strain gage measurements the data is adjusted to have a mean response of zero. The deflection determined from the strain gage signals and camera images were highly correlated.

The normalized expected mean squared response, $E[r^{*2}]$ of the system is determined using

$$E[r^{*2}] = E[y^{*2}] + E[z^{*2}] \tag{6}$$

where $E[y^{*2}]$ and $E[z^{*2}]$ are the expected mean squared deflection in the y and z direction. The deflections are normalized by the impeller diameter; $y^* = \frac{y}{D}$ and $z^* = \frac{z}{D}$.

Experimental Results

Tests were conducted in various fluid mixtures with initial viscosities: a) $\mu_1 \approx 50\ cP$, b) $\mu_2 \approx 100\ cP$ and c) $\mu_3 \approx 500\ cP$. Trials were conducted in both counter clockwise and clockwise directions for rotational speeds ranging from 148 rpm to 410 rpm in 10 and 20 rpm intervals. Measurements were recorded in series of increasing and decreasing rotation speed to identify if there was a hysteresis effect. The reversal of radial direction has the effect of reversing the axial thrust of the impeller from compressive (counter clockwise, CCW) to tensile (clockwise, CW).

Table 3. FLUID VISCOSITIES FOR EACH TRIAL.

With Baffles			
Compressive Axial Loading			
	a) $\mu \approx 40\ cP$	b) $\mu \approx 100\ cP$	c) $\mu \approx 500\ cP$
rpm	148-390	148-390	148-390
Ω^*	0.45-1.19	0.45-1.19	0.45-1.19
Re	454-1319	3678-10185	1907-5769
Tensile Axial Loading			
	a) $\mu \approx 50$	b) $\mu \approx 100$	c) $\mu \approx 500$
rpm	148-410	148-410	148-410
Ω^*	0.45-1.25	0.45-1.25	0.45-1.25
Re	382-1348	4861-15413	1764-5874

Experimental results for $E[r^{*2}]$ using a standard pitched blade impeller with baffles are plotted in figure 3. The results for a shaft with a compressive axial load, ($\Omega^* > 0$) show a peak at a frequency ratio of $\Omega^* = 0.74$ for all three test fluids. This is considered the first critical speed. The amplitude at the critical speed decreases with increased viscosity. In the supercritical region the amplitude remained approximately constant. The results for the tensile case shown in figure 3 ($\Omega^* < 0$) do not indicate a critical speed and the mean squared amplitude continued to increase as the frequency ratio was increased. Increased viscosity caused the amplitude of the mean squared response to decrease. Figure 3 b) also shows the results for a 4-blade impeller without pitch. This impeller does not produce axial thrust and yields symmetric results for both directions of rotation.

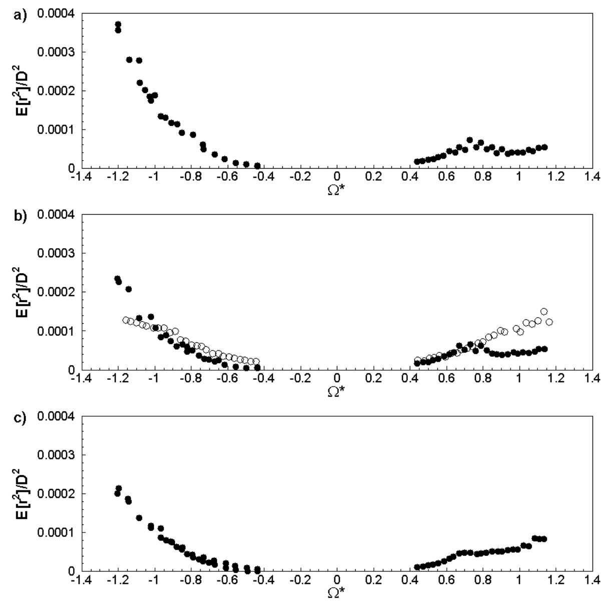

Figure 3. NORMALIZED SHAFT DEFLECTIONS FOR A 4 BLADE, 0.254 m DIAMETER IMPELLER WITH TENSILE ($\Omega^* < 0$) AND COMPRESSIVE ($\Omega^* > 0$) SHAFT LOADING IN THREE TEST FLUIDS: A) $\mu \approx 40\ cP$; B) $\mu \approx 100\ cP$; and C) $\mu \approx 500\ cP$. 4 BLADE, 0.254 M WITHOUT PITCH; ○.

Figure 4 shows the orbits for the impeller with tensile axial loading in a test fluid with $\mu \approx 50\ cP$ at four rotational speeds. Each data point is separated by 60° of rotation for 135 revolutions. In both directions the displacements were normally distributed; the skewness and kurtosis of the deflections for each orbit are listed in table 4.

Figure 5 shows the power spectral density (PSD) of the displacement in the y-direction for the four trials shown in figure 4. These PSD plots were normalized by their corresponding rotational speeds and constructed from the strain gage data that was sampled at 500 Hz and filtered at 250 Hz. These PSD diagrams show that the majority of the energy was contained in the frequencies $\omega^* < 1$. Each plot in figure 5 shows a rise in power near a value that coincides with $\frac{\omega}{2\pi} = 60\ Hz$ that is thought to be electrical noise.

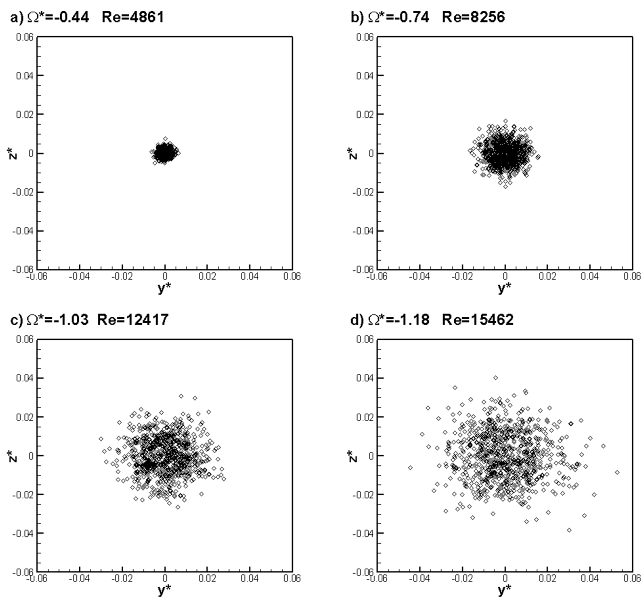

Figure 4. CAMERA DATA SHOWING THE ORBITS FOR A 4 BLADE, 0.254 m PITCHED BLADE IMPELLER WITH TENSILE LOADING IN A TEST FLUID WITH A VISCOSITY OF 40 cP. DATA POINTS ARE SPACED AT INTERVALS OF 60° OF IMPELLER ROTATION.

CFD SIMULATIONS

A Computational Fluid Dynamics (CFD) study was completed for the model geometry using the commercial solver, ANSYS CFX. This was done with the objective of supplementing experimental results in regard to the fluid forces acting on the rotating impeller. The computational domain included a rotating frame attached to the impeller and a stationary frame attached to the baffles and tank walls to permit ease of meshing. Time stepping was first order accurate with an increment of 1 ms or 1.4° of impeller rotation at 224 rpm. The unstructured finite element mesh used in the study included 1.3M elements and 250K nodes. Each revolution of the impeller required 24 hours of CPU time on 8 parallel processors. Simulations were conducted for 30 revolutions to establish a statistically steady state for the fluid forces and then an additional 32 revolutions were computed to form the basis of force spectral densities and average forces and moments used in the present study. Current simulations had a Reynolds number, $Re = \frac{\rho \Omega D^2}{\mu} = 270 * 10^3$. Simulations were performed for no orbit, synchronous orbit and 3 subsynchronous orbit speeds. The orbit amplitude was 10% of the blade baffle clearance. The time series of force on the impeller was random and statistically independent of the angular impeller location. A summary of the simulation results for the no orbit simulation is shown in Table 5. The average power number, N_p, of this simulation matched the experimentally determined value giving confidence in the average values of axial thrust and power spectral density of the horizontal forces.

Table 4. STATISTICS OF ORBITS.

Ω^*	Dir	Skewness	Kurtosis
0.44	y	-0.088	2.864
	z	0.377	2.973
0.74	y	-0.05	2.615
	z	0.106	2.804
1.03	y	-0.06	2.84
	z	0.039	2.786
1.18	y	-0.244	3.257
	z	0.091	2.677

Table 5. CFD RESULTS

$N_{p_{CFD}}$	1.51
$C_{T_{CFD}}$	0.018
$\overline{\left(\frac{f_{y_{CFD}}}{\rho \Omega^2 D^4}\right)^2}$	$1.12 * 10^{-6}$
$\overline{\left(\frac{f_{z_{CFD}}}{\rho \Omega^2 D^4}\right)^2}$	$9.92 * 10^{-7}$

DYNAMIC MODEL

Governing Equations

A free body diagram of a cantilever mixing shaft with a standard pitched blade impeller is shown in figure 6. This diagram shows a simplified sketch of the forces that are caused by both the dynamics of the shaft and the fluid flow surrounding the impeller. The equation of motion for a rotating shaft can be represented as [8]

$$[M]\{\ddot{r}\} + [C]\{\dot{r}\} + [K]\{r\} = \{f(t)\} + U\{r_0\} + V\{\dot{r_0}\} \quad (7)$$

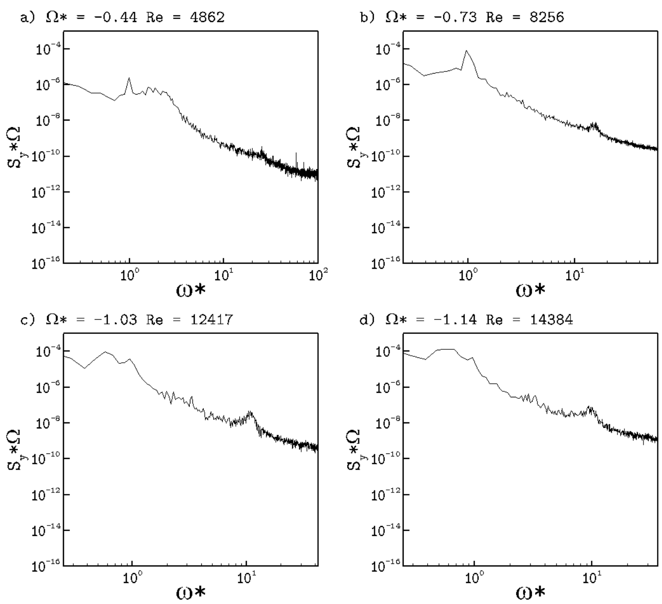

Figure 5. POWER SPECTRAL DENSITY OF THE SHAFT POSITION ($y^* = \frac{y}{D}$) IN THE y DIRECTION FOR A 4 BLADE, 0.254 m DIAMETER PITCHED-BLADE IMPELLER WITH TENSILE AXIAL LOADING IN A TEST FLUID WITH A VISCOSITY OF 40 cP.

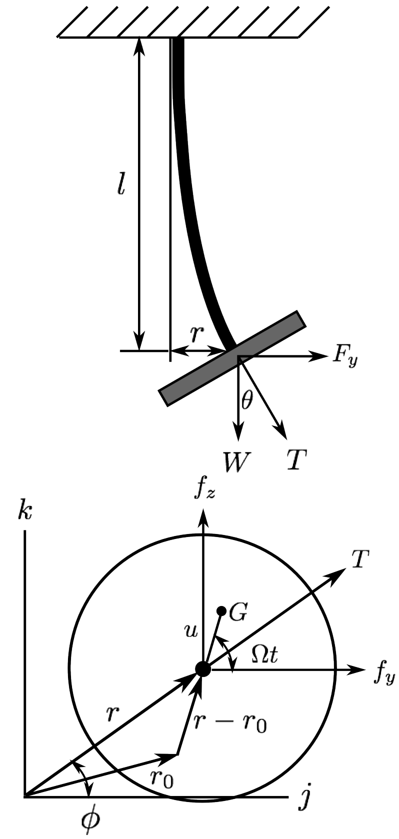

Figure 6. ROTATING MIXING SHAFT WITH FORCES AND MOMENTS.

where vector $\{r\}$ is the displacement from the axis of rotation in the horizontal plane

$$\{\mathbf{r}\} = \begin{Bmatrix} y \\ z \end{Bmatrix} \tag{8}$$

and $|\mathbf{r_0}|$ is the geometric misalignment which is taken to be the distance from the geometric center of the impeller to the center of rotation at zero rotational speed.

Expanding equation 7 into matrix form leads to the following [8]

$$\begin{aligned} &\begin{bmatrix} m_s+m_f & 0 \\ 0 & m_s+m_f \end{bmatrix} \begin{Bmatrix} \ddot{y} \\ \ddot{z} \end{Bmatrix} + \begin{bmatrix} c_s+c_f & 0 \\ 0 & c_s+c_f \end{bmatrix} \begin{Bmatrix} \dot{y} \\ \dot{z} \end{Bmatrix} \\ &+ \begin{bmatrix} k_s+k_a-k_r & k_c+k_\beta-k_\tau \\ -k_c-k_\beta+k_\tau & k_s+k_a-k_r \end{bmatrix} \begin{Bmatrix} y \\ z \end{Bmatrix} \\ &= m_s u \Omega^2 \begin{Bmatrix} \cos(\Omega t) \\ \sin(\Omega t) \end{Bmatrix} + \begin{bmatrix} c_s & 0 \\ 0 & c_s \end{bmatrix} \begin{Bmatrix} \dot{y}_0 \\ \dot{z}_0 \end{Bmatrix} \\ &+ \begin{bmatrix} k_s+k_a & k_c \\ -k_c & k_s+k_a \end{bmatrix} \begin{Bmatrix} y_0 \\ z_0 \end{Bmatrix} + \begin{Bmatrix} f_y \\ f_z \end{Bmatrix} \end{aligned} \tag{9}$$

The non-diagonal terms in the stiffness matrix of equation 9 represent coupling between the two systems of equations. The forcing function on the right side of the equation includes contributions from mass imbalance, misalignment and fluid forces.

Mass Matrix

Following the dictum of Adams [8] no non-diagonal terms are included in the mass matrix since they would produce instabilities at high rotational speed which are not consistent with observation [8]. Experiments conducted by Walston [17] reported that fluid damping and added mass had an effect on the amplitude of the shaft vibration. The author also showed that the critical speed will be noticeably lower for a rotating disk that entraps fluid within itself.

The mass of the impeller, m_s and the added fluid mass, m_f both contribute to the mass matrix. The added fluid mass was modeled as

$$m_f = \rho \, \forall \tag{10}$$

where $\forall$ is the displaced volume of the impeller. The ratio $\frac{m_f}{m_s} = 0.11$ for the present case.

Damping Matrix

The damping matrix includes the internal damping of the shaft and bearing system and the hydrodynamic damping. The structural damping factor is $c_s = 4.8824\ \frac{N*sec}{m}$ or $\zeta_s = 0.045$ and was directly measured using a bump test (without rotation) in air. Vance [18] models the hydrodynamic damping on the impeller as

$$F_{dv} = -c_f \begin{Bmatrix} \dot{y} \\ \dot{z} \end{Bmatrix} \tag{11}$$

Note that the hydrodynamic damping is independent of $\{r_0\}$. To determine the value of c_f a non-rotating impeller was bumped in 40 cP and 519 cP fluid. The result was a fluid damping of $c_f = 3.32\ \frac{N*sec}{m}$ and a fluid damping ratio of $\zeta_f = 0.06$. A non-rotating impeller in test fluid experienced a total damping factor of $\zeta_s + \zeta_f = 0.11$. Vance [18] also describes a nonlinear "aerodynamic" model that will not be considered in this study.

Stiffness Matrix

Diagonal Components The elastic force due to the deflection of the shaft from $\{\mathbf{r_0}\}$ was determined using the structural stiffness. The stiffness for the present shaft was $k_s = 1649\ \frac{N}{m}$ which was measured in a static horizontal position.

The presence of axial loads on the shaft can alter the structural stiffness [14]. The axial loads result from the vertical component of the impeller thrust, $T = C_T \rho D^4 \Omega^2 \cos(\theta)$, and the net weight. The additional stiffness is represented by k_a and is calculated as [14]

$$k_a = k_s \left(\frac{4l^2 (C_T \rho D^4 \Omega^2 + (m_s - \rho \cancel{V} + 0.5 \rho_s \cancel{V}_s) g)}{\pi^2 EI} \right) \tag{12}$$

where $\cos(\theta) \approx 1$, ρ is the fluid density, C_T is the coefficient for axial thrust produced by the impeller, ρ_s is the density of the shaft, $\cancel{V}_s$ is the volume of the shaft, D the impeller diameter, l is the length of the shaft, I is the moment of area and E is the modulus of rigidity. The thrust coefficient, C_T, may be either positive or negative depending on the direction of rotation. It was determined from computational fluid dynamic simulations to have a magnitude of $C_T = \pm 0.018$.

As the shaft deflects there is an angle between the bearing's axis of rotation and the impeller's axis of rotation which projects the impeller thrust onto the horizontal plane. This horizontal component of the impeller thrust, $C_T \rho D^4 \Omega^2 \sin(\theta)$, contributes to the effective stiffness of the shaft and is defined as

$$k_r = C_T \rho D^4 \Omega^2 \left(\frac{3}{2l} \right) \tag{13}$$

where $\sin(\theta) \approx \frac{3r}{2l}$ to be consistent with a static deflection curve. This assumption regarding the angle, θ, is rather uncertain and deserves closer scrutiny.

Non-Diagonal Components The first contribution to the non-diagonal stiffness is due to internal shaft friction [7] which is calculated as

$$k_c = c_s \Omega \tag{14}$$

where c_s is the structural damping coefficient measured in air.

The second contribution to the non-diagonal stiffness is due to torquewhirl [18] which is produced by the misalignment of the torque vector at the root of the shaft and the torque vector applied to the impeller by the fluid resistance. The added stiffness is calculated as [7]

$$k_\tau = \frac{\tau}{2l^2} \tag{15}$$

where τ is the torque applied to the impeller. This torque is determined using the power number as follows

$$\tau = \frac{N_p \rho \Omega^2 D^5}{(2\pi)^3} \tag{16}$$

where the value of N_p was determined by direct experimental measurement for the present impeller to be 1.37 which was consistent with the CFD results.

Alford's force is another contributor to the non-diagonal stiffness and is produced by the uneven pressure distribution on diametrically opposite impeller blades when the tip clearance is non-uniform. These forces act orthogonal to the deflection vector and can cause backward or forward whirl. The added stiffness is calculated as [8]

$$k_\beta = \frac{\beta \tau}{D_m L} \tag{17}$$

where β is an experimentally determined value in the range $-7 < \beta < 5$ [7,8,13] and can vary with operating conditions [13]. D_m is the the mean diameter of the compressor stage blade row and L is the radial length of the blades. It is unclear how to generalize this equation for mixing applications where the clearances are substantially larger and the baffles are periodic rather than continuous as in the case of turbomachinery casing. For the present study $-0.5 < \beta < 0.3$ provided stability in the range $-1 < \Omega^* < 1$. A value of $\beta = -0.1$ was chosen somewhat arbitrarily for the present simulations.

Excitation Force Matrix

The excitation force in this model includes the centrifugal forces due to mass eccentricity and geometric eccentricity and the fluid forces arising from the impeller rotation. The mass and geometric eccentricity were measured directly, these values are reported in table 6. The fluid forces were evaluated using a CFD simulation of the experimental model geometry, see table 5. The simulated fluid motion in the mixer and the resulting forces acting on the impeller were random with a typical sample power spectral density for the y component of force shown in figure 7. This sample was based 32 shaft revolutions. It was also observed that this random fluid force is statistically equal and uncorrelated in the y and z directions. The power spectral density was modeled as

$$S_{f_{y,z}}(\omega) = \begin{cases} 6.43 * 10^{-9}\left(\frac{\rho^2\Omega^4 D^8}{(m_s\Omega D)^2}\right) & \text{if } |\omega| \leq |3.0\Omega| \\ (|\omega|)^{-4}\left(\frac{6.43*10^{-9}}{3.0\Omega^{-4}}\frac{\rho^2\Omega^4 D^8}{(m_s\Omega D)^2}\right) & \text{if } |\omega| > |3.0\Omega| \end{cases} \quad (18)$$

which corresponds to the dashed line in figure 7. It is assumed that $S_{f_{y,z}}$ is independent of Re and therefore the amplitude increases as Ω^4 and the bandwidth increases as Ω.

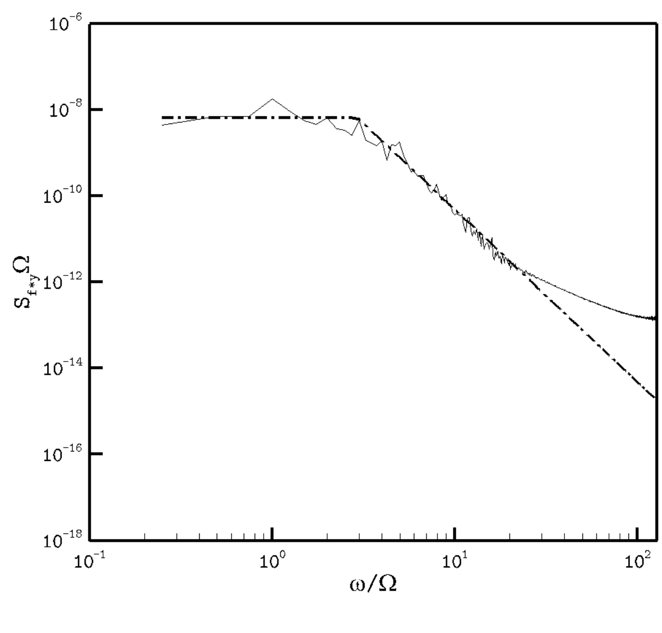

Figure 7. NORMALIZED POWER SPECTRAL DENSITY OF THE RANDOM FLUID FORCE IN THE y DIRECTION ON AN IMPELLER AT $\Omega = 23.45\ \frac{rad}{sec}$, CFD: —, MODEL EQ. 18: - - -.

Normalized Equation of Motion

Equation 9 was normalized by dividing by m_s and substituting: $\omega_{nb} = \sqrt{\frac{k_s}{m_s}}$, $2\zeta_f\omega_{nb} = \frac{c_f}{m_s}$, $2\zeta_s\omega_{nb} = \frac{c_s}{m_s}$, $t^* = t\omega_{nb}$, $y^* = \frac{y}{D}$ and $z^* = \frac{z}{D}$. Where ω_{nb} is the measured natural bending frequency ($\frac{rad}{sec}$) and ζ_s, ζ_f are the damping ratios without shaft rotation in air and liquid respectively. The normalized system of equations have the form

$$[\bar{M}]\{\ddot{\mathbf{r}}^*\} + [\bar{C}]\{\dot{\mathbf{r}}^*\} + [\bar{K}]\{\mathbf{r}^*\} = \bar{\mathbf{f}} \quad (19)$$

where

$$[\bar{M}] = \begin{bmatrix} 1+n_1 & 0 \\ 0 & 1+n_1 \end{bmatrix} \quad (20)$$

$$[\bar{C}] = \begin{bmatrix} 2\zeta_s + p_1 & 0 \\ 0 & 2\zeta_s + p_1 \end{bmatrix} \quad (21)$$

$$[\bar{K}] = \begin{bmatrix} \bar{K}_{11} & \bar{K}_{12} \\ \bar{K}_{21} & \bar{K}_{22} \end{bmatrix} \quad (22)$$

$$\begin{aligned} \bar{K}_{11} &= 1 + q_1\Omega^*|\Omega^*| + q_2 - q_3\Omega^*|\Omega^*| \\ \bar{K}_{12} &= q_4\Omega^* + q_5\Omega^*|\Omega^*| - q_6\Omega^*|\Omega^*| \\ \bar{K}_{22} &= K_{11} \\ \bar{K}_{21} &= -K_{12} \end{aligned} \quad (23)$$

$$[\bar{f}] = \begin{bmatrix} \frac{u}{D}\Omega^{*2}\cos(\Omega^* t^*) + (1+q_1\Omega^*|\Omega^*|)\frac{|r_0|}{D}\cos(\Omega^* t^*) + \frac{f_y}{m_s\omega_n^2 D} \\ \frac{u}{D}\Omega^{*2}\sin(\Omega^* t^*) + (1+q_1\Omega^*|\Omega^*|)\frac{|r_0|}{D}\sin(\Omega^* t^*) + \frac{f_z}{m_s\omega_n^2 D} \end{bmatrix} \quad (24)$$

and

$$\{\mathbf{r}^*\} = \begin{Bmatrix} y^* \\ z^* \end{Bmatrix} \quad (25)$$

Values for input parameters and coefficients are listed in table 6 while equations for n, p and q are listed in table 7. Values for m_s, c_s, k_s, c_f, $m_s u$ r_0 and N_p were all experimentally measured but the thrust coefficient, C_T was determined through CFD simulations. The viscous damping coefficient, c_f was an average value measured for a stationary impeller during a bump test in 50 cP and 500 cP test fluids.

Table 6. MODEL PARAMETERS

Symbol	Model Value	Symbol	Model Value
m_s	1.8 (kg)	$m_s u$	$7.2 * 10^{-6}$ $(kg * m)$
c_s	4.9 $\left(\frac{N*sec}{m}\right)$	N_p	1.37
k_s	1637 $\left(\frac{N}{m}\right)$	C_T	0.018
y_0	0.0 (m)	c_f	2.7, 3.3, 4.0 $\frac{N*sec}{m}$
z_0	0.0005 (m)	β	-0.1

Table 7. MODEL COEFFICIENTS

Parameter	Definition	Value
n_1	$\frac{m_f}{m_s}$	0.1146
p_1	$\frac{2c_f}{m_s \omega_n}$	0.049, 0.061, 0.073
q_1	$\frac{4l^2 C_T \rho D^4 \omega_n^2}{\pi EI}$	$\pm 0.3202^*$
q_2	$\frac{4l^2 (mg+0.5\rho_s Alg)}{\pi EI}$	0.073
q_3	$\frac{3C_T \rho D^4}{2lm_s}$	$\pm 0.1257^*$
q_4	$\frac{2c_s}{m_s \omega_{nb}}$	0.09
q_5	$\frac{\beta N_p \rho D^5}{D_m L (2\pi)^3 m_s}$	-0.052
q_6	$\frac{N_p \rho D^5}{2l^2 (2\pi)^3 m_s}$	0.0052

* Note: Sign of constant depends on slope of impeller blades: negative for positive sloped blades and positive for negatively sloped blades

Stability and Natural Frequency

Transforming equation 19 into state space allows for an analytic solution for the eigenvalue problem. The eigenvalue problem is defined as

$$U\mathbf{r}^* = \lambda \mathbf{r}^* \tag{26}$$

where

$$U = \left[\begin{array}{c|c} 0 & I \\ \hline -\bar{M}^{-1}\bar{K} & -\bar{M}^{-1}\bar{C} \end{array}\right] \tag{27}$$

The eigenvalues λ are complex in the form

$$\lambda = \alpha + \psi i \tag{28}$$

where α is the damping and ψ is the natural frequency. The system is only stable if all of the real values of the eigenvalues are negative, $\alpha < 0$. Note that since $\overline{K}$ is a function of the shaft turning rate Ω the eigenvalues as well and the natural frequency depends on Ω.

Frequency Response

$H(\omega)$ is the transfer function of the system in the frequency domain and was found by taking the Laplace transform of equation 19 and arranging it in the form

$$[A]\{R(i\omega)\} = F_f(i\omega) \tag{29}$$

with

$$\begin{aligned} A_{11} &= -\bar{M}_{11}\omega^2 + \bar{C}_{11}\omega i + \bar{K}_{11} \\ A_{12} &= \bar{K}_{12} \\ A_{22} &= -\bar{M}_{22}\omega^2 + \bar{C}_{22}\omega i + \bar{K}_{22} \\ A_{21} &= \bar{K}_{21} \end{aligned} \tag{30}$$

Rearranging equation 29 as

$$R(i\omega) = A^{-1}F_f(i\omega) = H(i\omega)F_f(i\omega) \tag{31}$$

defines the transfer function as

$$H(i\omega) = \frac{1}{det(A)} \begin{bmatrix} A_{22} & -A_{12} \\ -A_{21} & A_{11} \end{bmatrix} \tag{32}$$

Mean Squared Response

For two uncorrelated random inputs [19]

$$\begin{aligned} E[y^{*2}] = &\int_{-\infty}^{\infty} |H_{11}(\omega)|^2 S_{fy}(\omega)\, d\omega \\ &+ \int_{-\infty}^{\infty} |H_{12}(\omega)|^2 S_{fz}(\omega)\, d\omega \end{aligned} \tag{33}$$

$$E[z^{*2}] = \int_{-\infty}^{\infty} |H_{21}(\omega)|^2 S_{fy}(\omega)\,\mathrm{d}\omega + \int_{-\infty}^{\infty} |H_{22}(\omega)|^2 S_{fz}(\omega)\,\mathrm{d}\omega \quad (34)$$

The power spectral density of the forcing function in the y and z direction are $S_{fy}(\omega)$ and $S_{fz}(\omega)$ respectively.

Model Results

Figure 8 shows the model damping and natural frequency results for three viscous damping coefficients: $c_f = 2.7$, 3.3 and 4.0. This range was selected to show the sensitivity to the fluid damping. Figure 8 a) shows the real part of the eigenvalues to be entirely negative which indicates stability within $-2 < \Omega^* < 2$. Figure 8 b) shows that the natural frequency decreased for $\Omega^* > 0$ and increased for $\Omega^* < 0$. This is a direct result of the axial loading caused by the pitched blades. For $\Omega^* = 0$, $\psi < 1$ because of the fluid added mass.

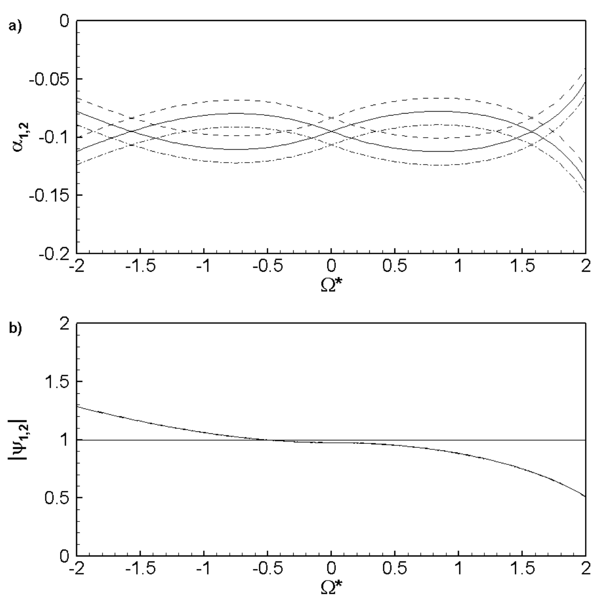

Figure 8. RESPONSE CHARACTERISTICS FOR A) SYSTEM DAMPING, B) NORMALIZED NATURAL FREQUENCY. LINES REPRESENT FLUID DAMPING COEFFICIENTS $c_f = 2.7\ \frac{kg}{sec}, --, c_f = 3.3\ \frac{kg}{sec}, —$ AND $c_f = 4.0\ \frac{kg}{sec}, - - -$

Values for $|H_{11}(i\omega)|$ and $|H_{12}(i\omega)|$ for three values of Ω^* and fluid damping coefficients are shown in figures 9 and 10 respectively. The transfer function for zero rotation (—) is representative of the response of the shaft experiencing plane bending while the transfer function for $\Omega^* = -1$ ($--$) represents a rotating shaft with a tensile axial load and $\Omega^* = 1$ (– - –) represents a shaft with a compressive axial load. For the zero rotation case $|H_{11}(i\omega)|$ peaks at $|\omega^*|$ slightly below 1 and $|H_{12}(i\omega)| = 0$. Peaks were produced at values $|\omega^*| > 1$ for $\Omega^* = -1$ while the transfer function for $\Omega^* = 1$ produced peaks at values below $|\omega^*| < 1$ for all damping coefficients.

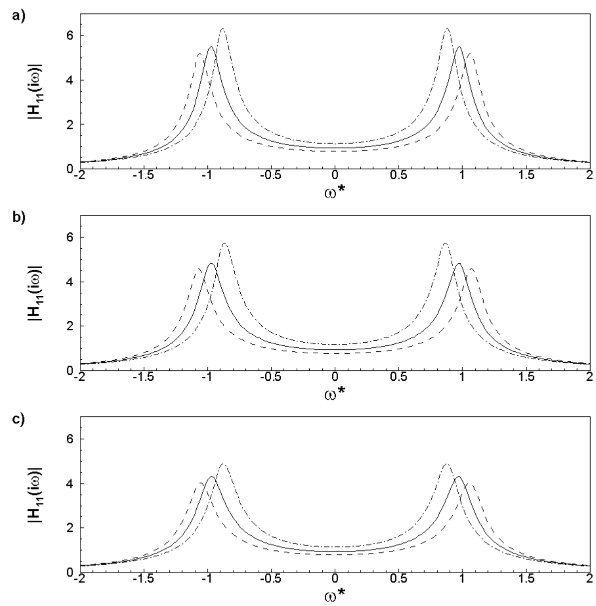

Figure 9. H_{11} FOR THREE DAMPING COEFFICIENTS: a) $c_f = 2.7\ \frac{kg}{sec}$, b) $c_f = 3.3\ \frac{kg}{sec}$ AND c) $c_f = 4.0\ \frac{kg}{sec}$. LINES INDICATE THREE ROTATION SPEEDS: $\Omega^* = 0, -, \Omega^* = -1, --$ AND $\Omega^* = 1, - - -$.

The expected mean squared response of the system calculated from equations 33 and 34 and using the random fluid force model of equation 18 is shown in figure 11.

DISCUSSION

The experimental results show that the impeller displacements are normally distributed random variable with a strong subsynchronous frequency content. The distribution of the displacements are also statistically axisymmetric. The mean square displacement shown in figure 3 depends strongly on shaft rotational speed but is asymmetric with respect to the direction of the shaft rotation. This asymmetry results from the 45° blade pitch and the change in direction of the axial thrust which accompanies a change in rotation direction.

The linear model presented used a combination of experimentally determined coefficients and fluid forces determined

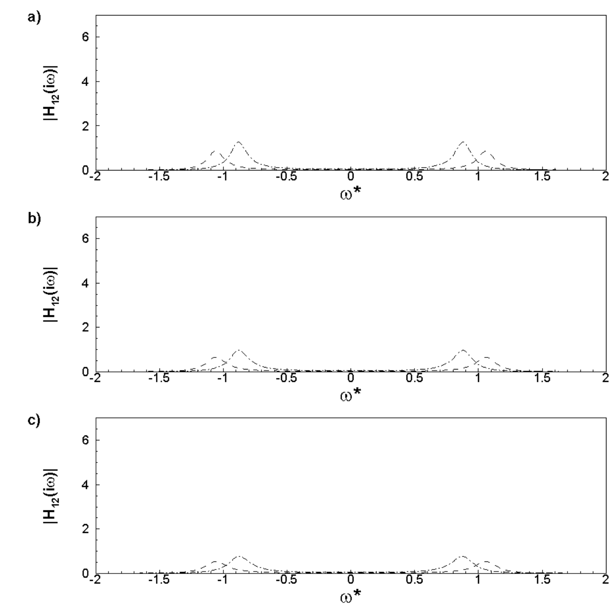

Figure 10. H_{12} FOR THREE DAMPING COEFFICIENTS: a) $c_f = 2.7\ \frac{kg}{sec}$, b) $c_f = 3.3\ \frac{kg}{sec}$ AND c) $c_f = 4.0\ \frac{kg}{sec}$. LINES INDICATE THREE ROTATION SPEEDS: $\Omega^* = 0, -$, $\Omega^* = -1, --$ AND $\Omega^* = 1, ---$.

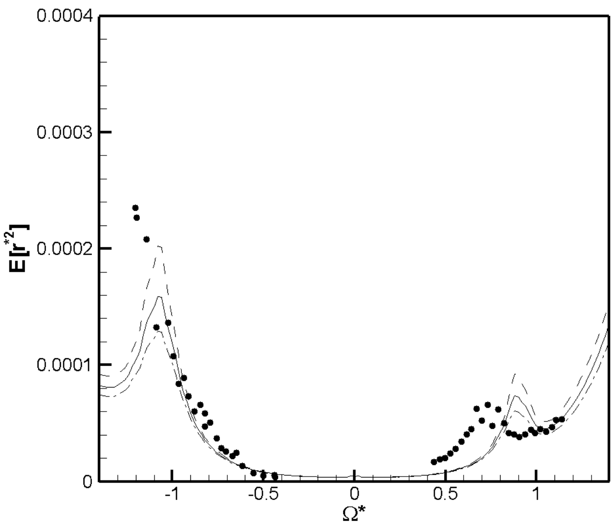

Figure 11. EXPECTED MEAN SQUARE RESPONSE FOR FLUID DAMPING COEFFICIENTS: $c_f = 2.7\ \frac{kg}{sec}, --$, $c_f = 3.3\ \frac{kg}{sec}$, — AND $c_f = 4.0\ \frac{kg}{sec}, ---$. EXPERIMENTAL RESULTS FROM FIGURE 3 b); ●.

from CFD simulations. These forces are random functions of time and are largely statistically axisymmetric which is consistent with experimentally observed displacements. Figure 11 compares the mean squared displacements predicted by the model to the data of figure 3 shows that the predictions are qualitatively correct. This includes the asymmetry of the critical speed for CW and CCW shaft rotation. This asymmetry in the natural frequency of the shaft increases with the square of rotation rate.

There are a number of assumptions that have been made in the derivation of the model that deserve closer scrutiny. Primary among them are the fluid mass, damping and stiffness coefficients. In particular the mass and damping coefficients were determined without consideration for the shaft rotation and as figures 8 and 11 show, the results are sensitive to the fluid damping coefficient. The fluid stiffness was based on Alford's force and did not consider any radial stiffness (diagonal component) that may be caused by the confinement due to the baffles and tank wall. However the model prediction proved to be relatively insensitive to the fluid stiffness as presently formulated.

A more rigorous approach to determining the hydraulic coefficients associated with impeller displacement would be to use CFD simulation results; research along these lines is ongoing. The main difficulty with this approach is the random nature of the fluid forces, even for the case of periodic orbits. This random nature requires a statistical approach to correlate the forces to displacements, velocities and acceleration that is very slow to converge. Given the demanding nature of CFD simulations new methods will have to be found to improve convergence rates.

SUMMARY

This paper presented experimental mean squared shaft deflections, sample orbits and power spectral density plots for a standard 45° pitched-blade impeller in a baffled mixing vessel as well as an analytical model for the stability, natural frequency and the expected mean squared response. The experimental results show that the deflection amplitude is asymmetric for CW and CCW shaft rotation and that the displacements were normally distributed in both the y and z directions. The power spectral density of the orbits shows that the majority of the energy is confined to subsynchronous frequencies.

CFD results were successfully used to estimate the power spectral density of the fluid forces on the impeller.

Model results for the mean square displacement were presented for a range of rotational speeds and produce similar trends to those found in the experimental results such as the effect of the shaft rotation rate and direction on the mean squared response and the first critical speed.

ACKNOWLEDGMENT

The authors acknowledge NOVA Chemicals' contribution to the design and construction of the apparatus and the financial support of NSERC and NOVA Chemicals. The CFD results were done Mr. Jiantao Zhang.

REFERENCES

[1] Oldshue, J., 1983. *Fluid Mixing Technology*. McGraw-Hill Publications Co., New York, N.Y.

[2] Hockey, R., and Nouri, J., 1996. "Turbulent flow in a baffled vessel stirred by a 60° pitched blade impeller". *Chemical Engineering Science,* **51**(19), pp. 4405–4421.

[3] Suzukawa, K., Mochizuki, S., and Osaka, H., 2006. "Effect of the attack angle on the roll and trailing vortex structures in an agitated vessel with a paddle impeller". *Chemical Engineering Science,* **61**(9), pp. 2791–2798.

[4] Chapple, D., Kresta, S., Wall, A., and Afacan, A., 2002. "The effect of impeller and tank geometry on power number for a pitched blade turbine". *Chemical Engineering Research and Design,* **80**(A4), pp. 364–372.

[5] Galletti, C., Paglianti, A., Lee, K., and Yianneskis, M., 2004. "Reynolds number and impeller diameter effects on instabilities in stirred vessels". *AIChE Journal,* **50**(9), pp. 2050–2063.

[6] Roussinova, V., Kresta, S., and Weetman, R., 2003. "Low frequency macroinstabilities in a stirred tank: Scale-up and prediction based on large eddy simulations". *Chemical Engineering Science,* **58**, pp. 2297–2311.

[7] Vance, J. M., 1987. *Rotodynamics of Turbomachinery*. John Wiley & Sons, Inc.

[8] Adams, M. L., 2001. *Rotating Machinery Vibration*. Marcel Dekker, Inc.

[9] Diken, H., 2001. "Non-linear vibration analysis and subharmonic whirl frequencies of the jeffcott rotor model". *Journal of Sound and Vibration,* **243**(1), pp. 117–125.

[10] Cohen, R., and Porat, I., 1984. "Influence of load torque on stability of rotor driven by flexible shaft". *Journal of Sound and Vibration,* **95**(2), pp. 151–160.

[11] Khader, N., 1995. "Stability of rotating shafts loaded by follower axial force and torque load". *Journal of Sound and Vibration,* **182**(5), pp. 759–773.

[12] Lee, J., and Yun, J., 1996. "Dynamic analysis of flexible rotors subjected to torque and force". *Journal of Sound and Vibration,* **192**(2), pp. 439–452.

[13] Storace, A. F., Wisler, D. C., Shin, H.-W., Beacher, B. F., Ehrich, F. F., Spakovszky, Z. S., Martinez-Sanchez, M., and Song, S. J., 2001. "Unsteady flow and whirl-inducing forces in axial-flow compressors: Part 1-experiment". *Journal of Turbomachinery,* **123**, pp. 433–445.

[14] Berger, T., Fischer, M., and Strohmeier, K., 2003. "Fluid-structure interaction of stirrers in mixing vessels". *Journal of Pressure Vessel Technology,* **125**(4), pp. 440–445.

[15] Mohamed, K. M., Gerber, A. G., and Holloway, G. A. L., 2009. "Modeling of hydrodynamic forces on a whirling mixing vessel stirrer including fluid-structure interaction". In Proceedings of the ASME 2009 Pressure Vessels and Piping Division.

[16] Kippers, N. R., and Holloway, G. A. L., 2009. "Vibration of standard pitched blade impellers in baffled mixing vessels". In Proceedings of the ASME 2009 Pressure Vessels and Piping Division.

[17] Walston, W., Ames, W., and Clark, L., 1964. "Dynamic stability of rotating shafts in viscous fluid". *Journal of Applied Mechanics*(3), June, pp. 291–299.

[18] Vance, J. M., 1978. "Torquewhirl - a theory to explain nonsynchronous whirling failures of rotors with high-load torque". *Journal of Engineering for Power,* **100**, pp. 235–240.

[19] Newland, D. E., 1993. *Random Vibrations, Spectral & Wavelet Analysis*, 3 ed. Longman Group Limited.